Kinetic Monte Carlo study of activated states and correlated shear-transformation-zone activity during the deformation of an amorphous metal

Kinetic Monte Carlo study of activated states and correlated shear-transformation-zone activity during the deformation of an amorphous metal

Eric R. Homer, David Rodney,* and Christopher A. Schuh†
Department of Materials Science and Engineering, Massachusetts Institute of Technology, Cambridge, Massachusetts, USA
(Received 4 October 2009; revised manuscript received 19 December 2009; published 19 February 2010)

Shear transformation zone (STZ) dynamics simulations, which are based on the kinetic Monte Carlo algorithm, are used to model the mechanical response of amorphous metals and provide insight into the collective aspects of the microscopic events underlying deformation. The present analysis details the activated states of STZs in such a model, as well as the statistics of their activation and how these are affected by imposed conditions of stress and temperature. The analysis sheds light on the spatial and temporal correlations between the individual STZ activations that lead to different macroscopic modes of deformation. Three basic STZ correlation behaviors are observed: uncorrelated activity, nearest-neighbor correlation, and self-reactivating STZs. These three behaviors correspond well with the macroscopic deformation modes of homogeneous flow, inhomogeneous deformation, and elastic behavior, respectively. The effect of pre-existing stresses in the simulation cell is also studied and found to have a homogenizing effect on STZ correlations, suppressing the tendency for localization.

DOI: 10.1103/PhysRevB.81.064204 PACS number(s): 61.43.Bn, 62.20.F−, 61.43.Dq

I. INTRODUCTION

Despite the significant number of studies devoted to the microscopic nature of deformation in amorphous metals, or metallic glasses, the underlying physics of deformation are not well established.[1] A number of models for microscopic deformation of glasses have been introduced,[2–8] with the shear transformation zone (STZ) originally proposed by Argon[3,4] emerging as a particularly useful mechanistic picture to describe the localized atomic motions that are observed in simulations.[9–12] STZs are groups of several dozen atoms that deform inelastically in response to an applied shear stress, with a displacement field in the shape of a quadrupole.[13–17]

Atomistic simulations have proven particularly useful for identifying the mechanistic events of metallic glass deformation and in fact atomistic analogs and simulations led directly to the development of the STZ theory of glass plasticity.[10,18] However, the time and length scales associated with such simulations are usually quite limited, making it difficult to analyze deformation on experimentally relevant scales. In contrast, continuum and phase field models built upon constitutive equations can capture the material behavior on experimentally relevant scales,[19–25] but can overlook the fundamental physical processes of the atomic motions associated with deformation.

The limited overlap between the time and length scales of the atomistic and continuum modeling approaches complicates the resolution of some important questions regarding the mesoscopic details of deformation in amorphous metals. For example, if the fundamental deformation mechanism in amorphous metals is the rearrangement of dozens or hundreds of atoms, as seen in atomistic simulations,[14,15,17] how do these individual events interact to effect macroscopic deformation? What spatial and temporal correlations exist between these individual events? How are these correlations affected by the local environment (e.g., stress, temperature, free volume)? Do STZs interact at all at high temperatures where metallic glasses exhibit stable viscous flow and common constitutive laws assume independent STZ activation?[1,26] More importantly, what sequence of events leads to shear localization, where material displacements on the order of micrometers develop over millisecond time scales and in confined bands that are only tens of nanometers thick?[27–32] Is this localization the result of cascades of correlated STZ activity or do smaller pockets of localized shear connect in a percolative fashion to form the shear bands?[33,34]

The effort to answer these questions may be facilitated through the use of mesoscale models, which have the ability to access intermediate length and time scales, allowing the connection between microscopic events and macroscopic deformation to be investigated.[35–37] A mesoscale modeling technique based on the dynamics of STZs was recently implemented by some of the present authors,[37] which considers deformation as a Markov chain of STZ activations that lead to deformation on a larger scale. In this technique, a simulated volume of material is partitioned into an ensemble of potential STZs which are mapped onto a finite element mesh. The stress and strain distributions in the system are solved at each step in the simulation using finite element analysis (FEA) and the kinetic Monte Carlo (KMC) algorithm is used in the selection of the STZ activations that make up the Markov chain. This modeling technique takes its inspiration from a model originally proposed by Bulatov and Argon,[35] but extends their work by accounting for the shape evolution of the system as well as allowing for complex loading geometries and boundary conditions thanks to the use of FEA. The results obtained from the mesoscale simulations follow the expected constitutive law for deformation at high temperatures and can, under some conditions, show localization into nascent shear bands during deformation at low temperatures.

The mesoscale modeling framework was developed in Ref. 37, which illustrated the model's ability to capture the basic modes of deformation of metallic glasses, but did not study collective STZ behavior. The purpose of the present

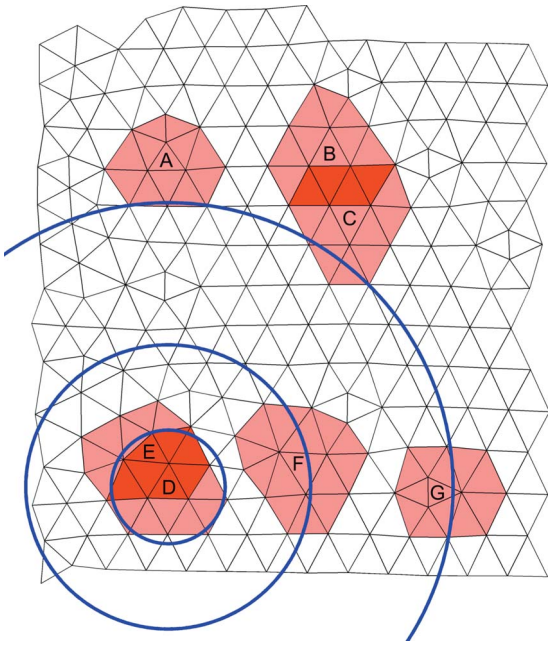

FIG. 1. (Color online) An irregular triangular mesh with several potential STZs highlighted; each is centered on an element and includes all surrounding elements. Overlap between STZs is denoted by the darker shading and circles with radii equal to 1, 2.5, and 5 times the STZ radius are centered on STZ "D" to indicate the distance between potential STZs.

paper is to revisit this simple model system with a goal of better understanding the conditions surrounding the selection and activation of STZs through additional analysis of the results obtained in Ref. 37. Of particular emphasis is the way in which STZs communicate with one another via the redistribution of stress fields, which leads to spatial and temporal correlations between activated STZs. Although spatiotemporal correlations have been studied at the atomic[14,15,36,38] and continuum[39] scales, here we explicitly explore such correlations among STZs in a mesoscale model of a deforming glassy system.

II. STZ DYNAMICS SIMULATIONS

In the STZ dynamics simulations described in Ref. 37, the finite element mesh representing the model glass is a two-dimensional irregular triangular mesh, with each element representing the center of a potential STZ. Each potential STZ also includes all the immediate surrounding elements (of which there are 12, on average), as illustrated by A, B, and C in Fig. 1. This method of mapping permits potential STZs to overlap (cf. B and C in Fig. 1) and represents one of innumerable possibilities for mapping STZs onto a mesh, the details and implications of which are discussed in Ref. 37 along with further details regarding the mesh and remeshing. Additional simulations involving a perfect triangular mesh show nearly identical results to those shown in Ref. 37 with an irregular triangular mesh, indicating mesh independence.

The standard KMC algorithm used to evolve the system requires the rate at which the different transitions in the system occur. The activation rate, $\dot{s}$, for a potential STZ to shear in one direction based on its local conditions (e.g., stress and temperature) is expressed as

$$\dot{s} = \nu_o \exp\left(-\frac{\Delta G}{kT}\right) \tag{1}$$

and is proportional to the Boltzmann probability for the system to be at the activation energy, ΔG, relative to the initial equilibrium state. The proportionality factor ν_o represents the attempt frequency, which is taken to be the Debye frequency, k is Boltzmann's constant, and the temperature, T, is uniform over the simulation cell. As proposed in Ref. 35, the activation energy, ΔG, for the STZ transition is modeled as

$$\Delta G = \Delta F - \tfrac{1}{2}\tau\gamma_o\Omega_o, \tag{2}$$

where the intrinsic barrier height for the reaction, ΔF, is biased by the local shear stress τ, which is obtained by volume averaging the stress over the elements which comprise each potential STZ. The activation volume, $\gamma_o\Omega_o$, of the STZ is comprised of the plastic strain increment associated with an STZ transformation, γ_o, and the volume of the STZ, Ω_o.

While Eq. (1) represents the activation rate for shearing an STZ in one direction, the implementation of the KMC algorithm provided in Ref. 37 allows STZs to shear in any direction in the plane of the simulation. The net STZ activation rate accounting for shear in any direction is given by

$$\dot{s} = \nu_o \exp\left(-\frac{\Delta F}{kT}\right) I_0\left(\frac{\tfrac{1}{2}\tau\gamma_o\Omega_o}{kT}\right), \tag{3}$$

where I_0 represents the modified Bessel function of the first kind of order zero. The KMC algorithm uses the cumulative activation rate for all potential STZs to select a single STZ to shear and to determine the residence time of the system in the current configuration. In this manner, the KMC algorithm effects the evolution of the ensemble of potential STZs to simulate the behavior of a metallic glass (see Ref. 37 for more details about the simulation technique).

As mentioned previously, the equilibrium stress and strain distributions at every step in the simulation are calculated using FEA. Because the STZ transformations are controlled by the KMC algorithm and the local plasticity of each transition is applied through the STZ shape change, the FEA only requires values for the elastic properties of the model glass, including the temperature-dependent shear modulus and Poisson's ratio. All the numerical values required for the STZ dynamics simulations are provided in Table I.

The simulations in Ref. 37 treated a model glass which is approximately 34.8 nm wide by 57.7 nm tall and which is free from any pre-existing stresses and strains. Six temperatures ranging from 300 to 800 K were considered, with stresses applied in a state of pure shear from 10 MPa to 4.75 GPa. The evolution of the system, containing more than 16 000 potential STZs, was followed over the course of more than 5000 STZ activations for each of 60 combinations of applied stress and temperature. The macroscopic response of the system (i.e., creep curves, system snapshots, etc.) are available in Ref. 37. In what follows, we analyze the STZ activity in these 60 simulations.

TABLE I. Parameters used in the STZ dynamics simulations.

Property	Symbol and value
STZ attempt frequency	$\upsilon_o = 1.0193 \times 10^{12}$ [s^{-1}]
Fixed barrier of activation energy	$\Delta F(T) = 1.175 \times 10^{-29}$ [J/Pa]$*\mu(T)$
STZ strain increment	$\gamma_o = 0.1$
STZ volume	$\Omega_o = 1.6$ [nm^3]
Temperature-dependent shear modulus	$\mu(T) = -0.004$ [GPa/K]$*T+37$ [GPa]
Poisson's ratio	$\nu = 0.352$

III. ACTIVATED STATE

A. Calculating the activated state

The KMC algorithm requires a model with which to calculate the activation energy, ΔG, of a transition or activated state. For an STZ dynamics model, the activation event corresponds to a local traversal between configurations, as shown schematically in Fig. 2(a). The model for ΔG for such a process must satisfy detailed balance[40–42] and the calculations should also be efficient. Bulatov and Argon[35] proposed a model for ΔG [Eq. (2)] that satisfies both these requirements for the case of STZ activation. This model is not immediately intuitive, so the details of the model along with points of contrast with respect to more traditional approaches used in KMC are discussed briefly below and in detail in the Appendix

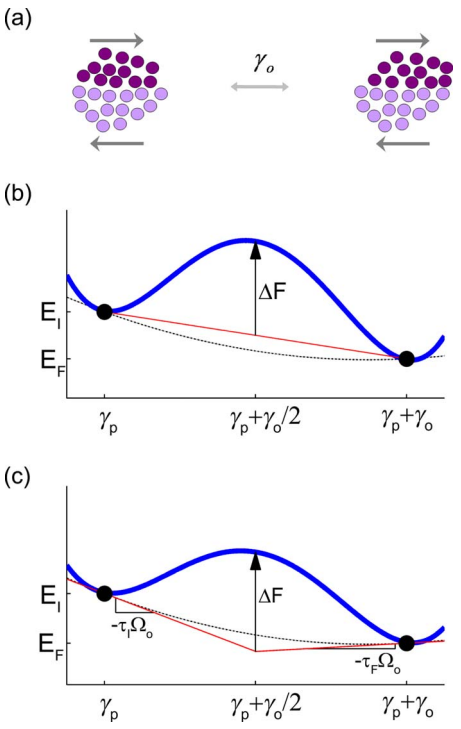

FIG. 2. (Color online) (a) Representation of the two states before and after the activation of an STZ. Illustration of the energy landscape and the method of identifying the activated state of an STZ in a (b) traditional KMC model where the activation energy, ΔG, is obtained by adding the fixed energy barrier ΔF to the average of the initial and final states and (c) the energy landscape for the model proposed by Bulatov and Argon (Ref. 35) where ΔG is obtained by adding ΔF to the projection of the slope (equal to the local shear stress) at the initial and final states. The variation in energy between the two states is given by dashed line and is the same in both (b) and (c).

Traditional methods used to calculate the activation energy, ΔG, for KMC simulations can be inefficient because they require knowledge of the final state for calculation. This is illustrated by the potential-energy landscape in Fig. 2(b) where a fixed barrier height, ΔF, is added to the average of the energy in the initial and final state. In the model proposed by Bulatov and Argon,[35] the activation energy is determined by adding the fixed barrier height, ΔF, to the slope of the potential energy at the initial state, which is equal to the local shear stress for the STZ, as illustrated in Fig. 2(c) and as defined in Eq. (2). This model is more efficient than traditional methods because it only requires knowledge of the initial condition and the contribution of continuously distributed shear planes to the STZ activation rate can be considered in a mathematically convenient form [Eq. (3)].

Before proceeding, we note that in the development of the KMC model in Ref. 37, the activation energy [Eq. (2) in the present paper] was written without a factor of $\frac{1}{2}$ in the second term. That paper followed the nomenclature convention more common in the experimental literature, subsuming the $\frac{1}{2}$ into the definition of the apparent activation volume. Here we have reintroduced the factor of $\frac{1}{2}$ to render the detailed balance calculation in the Appendix more transparent; updated model parameters relative to those provided in Ref. 37 are given in Table I. Of the model parameters given in Table I, $\mu(T)$, ν, and ν_o, represent experimentally obtained properties of a metallic glass, while $\Delta F(T)$ and Ω_o were obtained by fitting experimental data as described in Ref. 37.

B. Statistics of the activated state

At each of the KMC steps in the simulation, the algorithm has more than 16 000 potential STZs from which to choose to evolve the system. The statistics of these potential transitions are available in the density of potential activation energies, $\rho(\Delta G)$, and the corresponding probability density distribution, $p(\Delta G)$, defined as

$$p(\Delta G) = \frac{1}{Z}\rho(\Delta G)\exp\left(-\frac{\Delta G}{kT}\right), \tag{4}$$

where Z is the partition function. Both $\rho(\Delta G)$ and $p(\Delta G)$ are averaged over all the KMC steps to smooth out the effects of

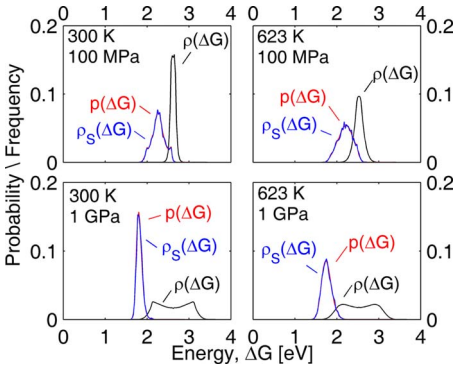

FIG. 3. (Color online) Statistics of the density of activation energies, $\rho(\Delta G)$, and the corresponding probability density distribution, $p(\Delta G)$, alongside the density of selected activation energies, $\rho_S(\Delta G)$, for four different simulations carried out under a combination of temperatures, 300 and 623 K, and applied stresses, 100 MPa and 1 GPa.

individual transitions that might be more abundant at different steps. We will also consider $\rho_S(\Delta G)$, the energy distribution of the transitions selected in the course of simulations. Figure 3 presents the measured distributions of $\rho(\Delta G)$ and $\rho_S(\Delta G)$ along with $p(\Delta G)$ calculated according to Eq. (4) for four simulations which cover two temperatures, 300 and 623 K, and two applied shear stresses, 100 MPa and 1 GPa.

It is important to recall that our KMC algorithm allows each STZ to shear in any direction, thus creating a continuum of transition states for each potential STZ. This is incorporated into the rate equation by calculating the maximum in-plane shear stress, $\tau_{\max}$, and then modulating that value by the sine of the angle relative to the direction of $\tau_{\max}$ as defined by

$$\Delta G = \Delta F - \tfrac{1}{2}\tau_{\max} \sin\theta \gamma_o \Omega_o. \tag{5}$$

It follows that the distributions of $\rho(\Delta G)$ are symmetric about the intrinsic barrier height, ΔF, and the contribution of each potential STZ is limited to $\pm\frac{1}{2}\tau_{\max}\gamma_o\Omega_o$, where energies below ΔF are for transitions in the direction of the local $\tau_{\max}$ and those above ΔF are opposed to it.

In calculating the distributions of $\rho(\Delta G)$ in Fig. 3, we have used 360 uniform increments of θ on the interval $[-\pi,\pi)$ and a bin size on ΔG of 0.025 eV. Therefore, at the lower applied stress of 100 MPa, the range of $\Delta F \pm \frac{1}{2}\tau_{\max}\gamma_o\Omega_o$ is small and the distributions of $\rho(\Delta G)$ at both temperatures, 300 and 623 K, are narrow and appear unimodal, obscuring the tendency to see an increased number of states at the limits. For the higher applied stress of 1 GPa, however, $\rho(\Delta G)$ appears bimodal on account of the increased magnitude of $\tau_{\max}$ which result in a spread of the data, accentuating the increased number of transitions with energy close to the limiting values of $\Delta F \pm \frac{1}{2}\tau_{\max}\gamma_o\Omega_o$.

While the temperature dependence of ΔF, defined in Table I, can be seen by the slight decrease in ΔF at higher temperatures, the temperature effects are more noticeable in the broadening of $\rho(\Delta G)$ at higher temperatures. The greater thermal energy available at these higher temperatures allows more transitions to take place, creating different states and more potential transitions of varying energies during the course of the simulation.

While $\rho(\Delta G)$ gives the distribution of all potential transitions that are enumerated in the KMC algorithm, the probability, $p(\Delta G)$, for picking a transition with energy ΔG is a competition between the number of transitions at that energy, $\rho(\Delta G)$, and the available thermal energy, kT, as in Eq. (4). In these simulations, the available thermal energy is small in comparison to the energy of the transitions, in the range of $\sim 0.02-0.07$ eV, making the lowest energy transitions the most likely to be selected. And indeed, in Fig. 3, it can be seen that although $\rho(\Delta G)$ spans a large range of energies, only the transitions corresponding to the lower portion of this range are probabilistically relevant. At 100 MPa and at both temperatures, $p(\Delta G)$ is only relevant over the lower half of the range of $\rho(\Delta G)$, which corresponds to shearing an STZ in the general direction of $\tau_{\max}$. At 1 GPa, however, only the transitions very close to the direction of $\tau_{\max}$ are likely to be selected. In all cases, the probability for picking an STZ opposed to the direction of $\tau_{\max}$ (where $\Delta G > \Delta F$) is near zero because the thermal energy required to activate these "backward" processes is too large. As expected, the transitions selected, $\rho_S(\Delta G)$, closely match the expectations based on $p(\Delta G)$, as shown by the virtually perfect overlap of these curves for all conditions in Fig. 3.

IV. STZ CORRELATIONS

Having detailed the activated state and the conditions that lead to the probabilistic selection of STZs, we turn our attention to an analysis of the correlations between the STZ activations in both space and time. An illustration of our approach can be seen in Fig. 1, where the highlighted STZs can be thought of as being activated or sheared in alphabetical order. We analyze the distance, r, between the center of each selected STZ and the following jth subsequent STZ activation. Our unit of distance is the average radius of an STZ and a reference for gauging the distance r between STZ "D" and the jth activation (i.e., E, F, G,…) that follows is given by the circles centered on D with radii of 1, 2.5, and 5 times the average STZ radius.

In some cases, it is instructive to use the time and distance between activations to simply calculate the number fraction of sequential STZ events that occur within a given radius of a previous STZ activation. In other cases, a richer view is offered by inspecting the time-dependent radial distribution function (TRDF) of STZ activations. The TRDF is given by

$$g(r,j) = \frac{n(r,j)}{q(r)}, \tag{6}$$

where $n(r,j)$ is constructed by binning the number of sequential activations as a function of r and j, and $q(r)$ is defined as

$$q(r) = \begin{cases} 1 & \text{if } r \le \dfrac{1}{2\pi dr\rho_{\mathrm{STZ}}} \\ 2\pi r dr \rho_{\mathrm{STZ}} & \text{if } r > \dfrac{1}{2\pi dr\rho_{\mathrm{STZ}}}, \end{cases} \tag{7}$$

where ρ_{STZ} represents the overall density of STZ activations, i.e., the total number of STZ activations per unit area. The

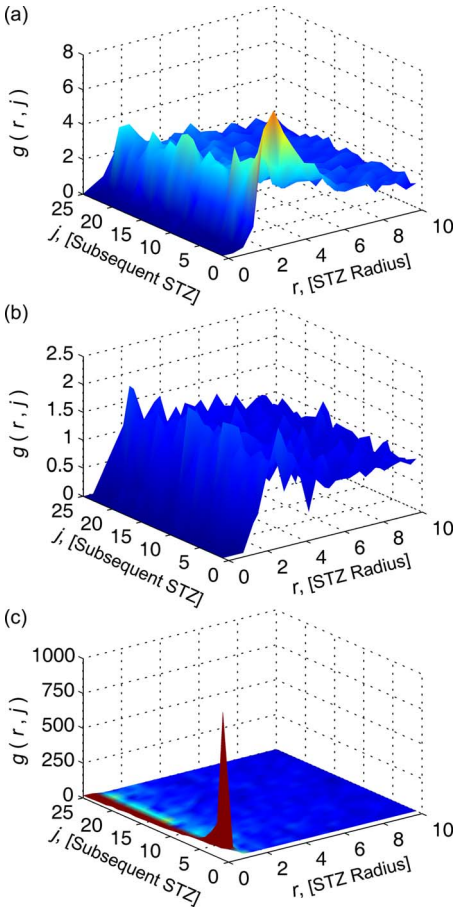

FIG. 4. (Color online) General behaviors in the TRDFs of STZ activation, where the three behaviors and their corresponding conditions are (a) nearest-neighbor STZ activation: high stress and low temperature, (b) independent STZ activation: high stress and high temperature, and (c) self-STZ activation: low stress and any temperature. The shading of all three surfaces uses the same color scheme, permitting comparison of the magnitudes of the different trends.

normalization quantity $q(r)$ represents a uniform STZ activation density and the piecewise form of Eq. (7) is introduced to prevent the divergence of $g(r,j)$ as $r \to 0$ for discrete systems such as ours. The size of the bins, dr, for the TRDFs analyzed here is approximately equal to half of the STZ radius.

A. General STZ correlation behaviors

An analysis of the 60 different simulations reveals three basic types of behavior that manifest under different combinations of applied stress and temperature. These behavior types are cataloged in Fig. 4 by the characteristic form of the TRDF they exhibit and are described below.

(a) "Nearest-neighbor STZ activation," which is observed for the simulations at high applied stress and low temperatures, is illustrated in Fig. 4(a). This behavior is characterized by an early, broad peak spanning roughly $r=1-5$, centered between about 2 and 3. As shown by the circles in Fig. 1 (which are located at $r=1$, 2.5, and 5), the peak breadth corresponds to activations in the immediate neighborhood of the first STZ, centered on what may be called the nearest-neighbor distance. The peak in the TRDF is generally 3–5 times the value for a uniform distribution and persists only for early times from the first STZ activation ($j \approx 1-3$) indicating that the frequency for immediate subsequent activation of a neighboring STZ is higher than that for uniform activation throughout the simulation cell (cf. STZs D, F, and G in Fig. 1). For values of r less than 1, however, $g(r,1) \sim 0$, indicating that the frequency for activating STZs that spatially overlap the original STZ (or for reactivating the original STZ itself) in subsequent steps is nearly zero (cf. STZs D and E in Fig. 1).

(b) "Independent STZ activation," which occurs under conditions of high applied stress and high temperatures, is illustrated in Fig. 4(b). In this behavior, the TRDF once again shows no preference for reactivation of STZs atop the first one, since again $g(r,j) \sim 0$ at $r<1$. However, at higher temperatures, the tendency for activation of neighboring STZs is lost; there is no longer a discernible peak elsewhere in the TRDF, which is valued near unity for all $r>1$ and $j \geq 1$. This constant value of the TRDF indicates that all STZs throughout the simulation cell are equally likely to activate; there is no correlation among STZs.

(c) "Self-STZ activation," which dominates at low applied stress and any temperature, is illustrated in Fig. 4(c). Unlike the previous behaviors, Fig. 4(c) exhibits an extremely pronounced and sharp peak in the TRDF at $r=0$ and for early times ($j<4$). The spatial extent of the peak is limited to $r \leq 1$, indicating a large preference for a second STZ activation atop the first. For all other $r>1$ and all j, $g(r,j) \sim 1$, indicating zero preference for correlated STZ activity at large distances.

The three behaviors identified in Fig. 4 coincide with three different types of macroscopic deformation that are easily identifiable on a deformation map. Namely, the nearest-neighbor STZ activation occurs under conditions which lead to inhomogeneous deformation, independent STZ activation occurs under conditions which lead to homogeneous deformation, and self-STZ activation occurs, in general, under conditions which are identified with nominally elastic behavior.[37]

The connection between nearest-neighbor STZ activation and macroscopic inhomogeneous deformation is relatively straightforward. At high stresses, the system is most likely to activate all STZs in the direction of the applied stress. Once one STZ is activated, it raises the stress in all neighboring STZs, and where the available thermal energy is low at low temperatures, the frequency for nearest-neighbor STZ activation is increased, leading to localized deformation. For independent STZ activation, which occurs at high applied stress and high temperature, the available thermal energy is now sufficient to enable STZ activation at other positions even though the stress in the neighboring STZs is high.

Self-STZ activation is linked to the elastic regime for two reasons. First, at low temperatures, there is insufficient thermal relaxation to accommodate a single STZ operation and at low stresses, there is insufficient tendency for a single STZ to trigger nearest-neighbor activations; thus, the most likely response of the system is for each STZ activation to be

nearly instantaneously reversed. Second, the activation energy associated with most of these transitions is very large and when little thermal energy is available, this leads to large KMC step times and thus extremely slow strain rates, which are not experimentally relevant. Thus, when self-STZ activation behavior is observed, the system evolves very slowly and the effect of forward plastic events is quickly diminished by backward ones at essentially the same location, indicating that the system is more likely to remain effectively elastic.

While the general types of STZ activity identified in this section are instructive, neither all of their features nor the transitions between them are well defined as yet. A more detailed analysis follows, in which we find it useful to decompose the observed correlations into the spatial and temporal components.

B. Spatial correlation analysis

To better understand the spatial component of the STZ correlations identified as self-STZ activation and nearest-neighbor STZ activation, the values for the TRDF of STZ activity may be plotted as contours over the range of available temperatures and applied stresses. These contour plots of $g(r,j)$ are presented in Fig. 5 where Fig. 5(a) corresponds to the value of the self-STZ activation peak at $r=0$ and Fig. 5(b) corresponds to the value of the nearest-neighbor STZ activation peak at $r=2.5$. In both cases, we consider only $j=1$ to focus solely on the first subsequent STZ activation. We observe that the self-STZ activation behavior is dominant at low stress and while it extends over the entire temperature range covered in Fig. 5(a), it is especially important at low temperatures where the magnitudes of the contours are significantly higher. These observations are in good agreement with the proposed connection between this STZ behavior and the elastic range, which is indeed prevalent at low stresses and temperatures. The extension of this behavior to the higher temperatures is somewhat unexpected because in this range, creeplike homogeneous flow is expected. This issue can be resolved by examining the number fraction of subsequent STZ activations that can be identified with self-STZ activation.

The number fraction of subsequent STZ activations that are associated with self-STZ activation and nearest-neighbor STZ activation are shown in Figs. 5(c) and 5(d) for events which fall in the range $0\leq r\leq 1$ and $1<r\leq 5$, respectively. Now, by comparing Figs. 5(c) and 5(a), we observe that although the peak in the TRDF for self-STZ activation persists to high temperatures at low stresses, the fraction of events contributing to that peak is very low indeed. The reason for the apparent discrepancy is that the TRDF tends to accentuate information near the origin ($r=0$), where very few events are needed to cause a peak to emerge. In contrast, Figs. 5(b) and 5(d) for the nearest-neighbor STZ activation behavior show a closer agreement to one another. In this case, larger values of r are of interest and the TRDF accordingly requires larger numbers of events before a peak emerges.

As an additional point of reference for establishing the regions for the different behaviors of correlated STZ activity, a simple simulation was carried out to calculate the probabilities for self-STZ activation or nearest-neighbor STZ activation following the activation of a single STZ. In other words, a single STZ was activated in a simulation cell with no internal structure (no stress distribution) and afterwards, the probability for activating that same STZ or a nearest-neighbor STZ was calculated over a range of temperatures and applied stresses. These probabilities can be seen in Figs. 5(e) and 5(f) for the self-STZ activation and nearest-neighbor STZ activation probabilities. It is noted that the probabilities for these regions are higher than the observed fractions in Figs. 5(c) and 5(d); however, this can be attributed to the fact that the probabilities are calculated for a cell in which there is only one STZ activated. On the other hand, when a distribution of stresses and strains is present due to a prior history of STZ activity, the competing probabilities of many other possible events decreases the relative probability for correlated STZ activity; it does not, however, remove it altogether.

One final point of interest in Figs. 5(b), 5(d), and 5(f) is that the probability or frequency for nearest-neighbor STZ activation drops off at very high stresses. This results from

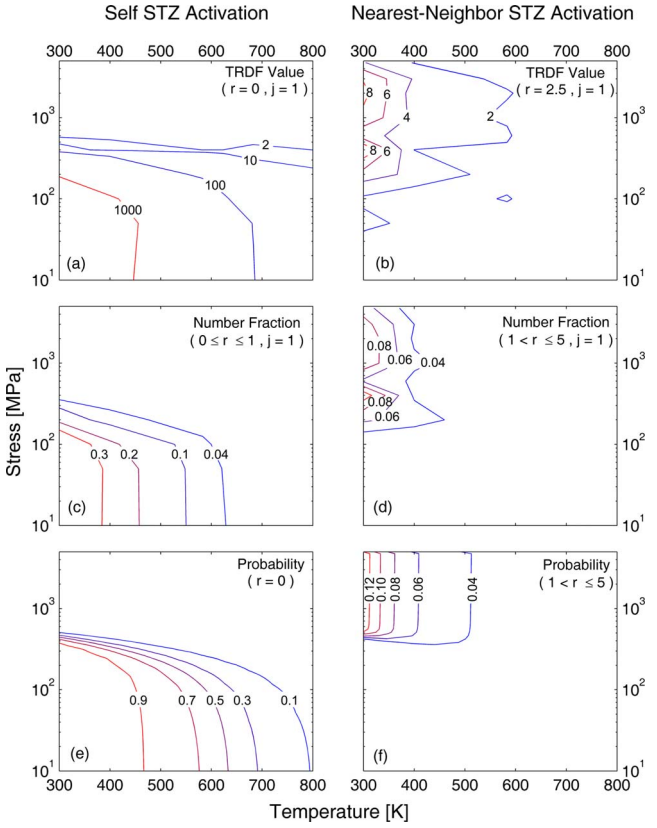

FIG. 5. (Color online) Contour plots of several different statistical measures that capture STZ correlations over a range of applied stresses and temperatures: (a) the TRDF values of self-STZ activation, $g(r=0,\ j=1)$, and (b) of nearest-neighbor STZ activation $g(r=2.5,\ j=1)$, (c) number fraction of subsequent, $j=1$, self-STZ activation events within the range $0\leq r\leq 1$, and (d) number fraction of subsequent nearest-neighbor STZ activation events within the range $1<r\leq 5$. Contour plots of the probability of (e) self-STZ activation and (f) nearest-neighbor STZ activation following the activation of a single STZ in a simulation cell over a range of temperatures and applied stresses.

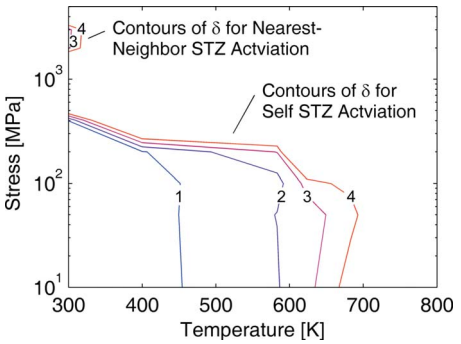

FIG. 6. (Color online) Contour plot of the time constant, δ, which measures the time decay of the TRDF correlation peaks at $r=0$ for the self-STZ activation correlation and at $r=2.5$ for the nearest-neighbor STZ activation correlation. Regions not enclosed by the contours did not provide a satisfactory fit for δ.

the fact that the magnitude of the stresses resulting from individual STZs is small in comparison to the very high applied stress, removing the preference for nearest-neighbor STZ activation.

C. Temporal correlation analysis

In examining the general behaviors of correlated STZ activity in Fig. 4, we see that where there is a significant peak, $g(r,j)>2$, in the TRDF, there is also a time dependence to the peak. These peaks appear to exhibit a general first-order decay and as such, the time dependence of the correlations can be quantified with a first-order time constant. The time constant δ is measured in KMC steps, j, and gives the number of subsequent STZ activations over which the likelihood of correlated STZ activity decays by $1-e^{-1}$.

Because temporal correlations only exist when a peak is evident in the TRDF, we focus our measurements of δ on two values of r, 0 and 2.5, which correspond to the self-STZ activation and nearest-neighbor STZ activation behaviors, respectively. In order to find the best fit for δ, an exponential function is set to match the initial peak height at $j=1$ and the average peak height at $j=20-25$ and then a least-squares method is used to determine an appropriate value for δ. Those values of δ obtained from reasonable exponential fits ($R^2>0.8$) are presented in Fig. 6 and labeled with the behavior corresponding to the position of the fitted peak, self-STZ activation ($r=0$), and nearest-neighbor STZ activation ($r=2.5$). As expected, the regions enclosed by the two different behaviors shown in Fig. 6 match reasonably with those shown in Fig. 5. In all cases, the value of δ is always less than five STZ activations, indicating that the lifetime for correlations between STZ activations is very short-lived.

Physically, this short life span of correlated STZ activity implies that the probability of observing a large string of correlated events is negligible. Indeed, in all of the 60 simulations, a string of more than two sequential nearest-neighbor STZ activations was rarely observed. The reason for this lies in the fractions and probabilities for nearest-neighbor STZ activation shown in Figs. 5(d) and 5(f), respectively, where the probability for activating a nearest-neighbor STZ is systematically less than 10%. This means that the probability to observe a string of three correlated events is approximately 1% or less.

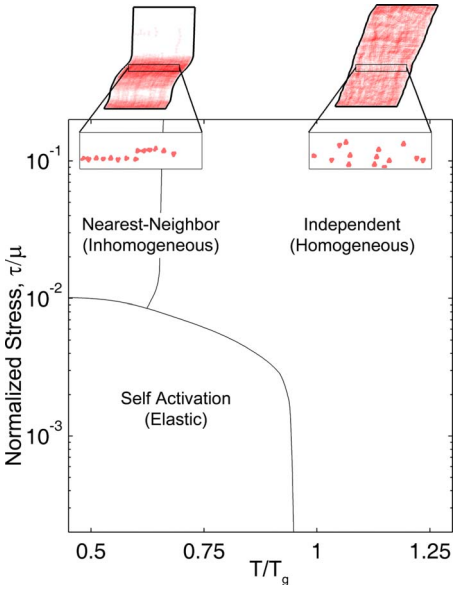

FIG. 7. (Color online) STZ correlation map delineating the different regions where nearest-neighbor STZ activation, independent STZ activation, and self-STZ activation occur. The corresponding macroscopic modes of deformation are also included in parentheses.

D. STZ correlation map

An STZ correlation map can be compiled from the above analysis to illustrate how the general STZ correlation behaviors are governed by the externally imposed applied stress and temperature. This map can be seen in Fig. 7, where the different regions denote the conditions under which self-STZ activation, nearest-neighbor STZ activation, and independent STZ activation are most likely to occur. As can be seen in Figs. 5 and 6, none of the regions corresponding to the different STZ correlations match exactly, so qualitative boundaries for these regions have been identified in Fig. 7. Furthermore, Fig. 7 is provided in normalized units for comparison to a wider range of metallic glasses, with the stress normalized by the temperature-dependent shear modulus, $\mu(T)$, and the temperature normalized by $T_g=623$ K, a glass transition temperature close to that of many Zr-based bulk metallic glasses.[7] As mentioned previously, these regions coincide well with the different modes of macroscopic deformation that were observed in Ref. 37 and are commonly observed in experiments of metallic glasses, namely, elastic, inhomogeneous, and homogeneous, respectively. Of course, the boundaries between these regions are not rigid and there are occasional correlated events that occur outside the defined regions of correlated STZ activity. However, in general, the regions delineated in Fig. 7 accurately capture the microscopic STZ correlations (and align with the macroscopic modes of deformation) observed in the simulations.

V. MACROSCOPIC INHOMOGENEITY

The macroscopic nature of deformation in an amorphous metal is typically easy to discern in the limiting cases of

localized shear and perfectly homogeneous deformation. However, not all cases of deformation fall cleanly into one of these two categories and an objective measure to assess the degree of localization would be helpful. To do so here, we adapt an analysis approach useful for quantifying the size of deformation and relaxation events in atomistic simulations, called the participation ratio, which gives the fraction of atoms that participate in any given process.[43,44] We present a quantitative measure termed the "localization index," which while inspired from and similar in form to the atomistic participation ratio, can be used to quantify localization on a macroscopic level

$$\Gamma = 1 - \frac{\left(\sum_n \gamma_n^2\right)^2}{N\sum_n \gamma_n^4}, \tag{8}$$

where γ_n is the plastic strain accumulated through STZ activity in each of the N mesh elements of the simulation cell following deformation. The localization index, Γ, identifies the fraction of the cell that participates in the overall deformation, thus giving an objective measure for the degree of localization or inhomogeneity. The value of Γ will range from unity if all the strain is concentrated on an infinitely thin shear band to zero for deformation that is uniformly distributed across the entire simulation cell. We find that values below about 0.5 correspond to very homogeneous flow, with a superimposed background of noise (as expected in a disordered solid).

The value of Γ obtained by analyzing the 60 simulations is plotted in contours for fractions of Γ greater than 0.5 in Fig. 8. The value of γ_n in this case is the effective plastic strain[45] (in two dimensions) in each element, defined as

$$\varepsilon_{eff} = \sqrt{\tfrac{2}{3}\left(\varepsilon_{11}^2 + \varepsilon_{22}^2 + \tfrac{1}{2}\gamma_{12}^2\right)}, \tag{9}$$

where ε_{11}, ε_{22}, and γ_{12} represent the plastic strain in the x and y directions and the plastic shear strain, respectively. (Since the former two strains are small, using only the component γ_{12} in the direction of the applied stress yields nearly identical results.) As expected, the region of correlated nearest-neighbor STZ activation (cf. Figs. 5–7) is enclosed in a region of high Γ. This confirms that local correlations in STZ activity lead to localization on larger scales where visible regions of inhomogeneous deformation can be identified even if no large chain of sequential events is ever observed. On the other hand, the region of high Γ at low stresses and temperatures may seem unexpected since it corresponds to the elastic response of the material. The reason for this apparent discrepancy is that the nature of the inhomogeneity at low stresses is different than that at high stresses. At low stresses, the high value of Γ is due to small pockets of high strain in a sample that is otherwise uniformly deformed; these pockets are also the result of STZ activations that occur on unreasonable time scales, leading to apparently elastic deformation. Furthermore, it is noted that the high value of Γ at low stresses may be due to the fact that the magnitude of overall shear strain that has accumulated during the simulations is small and a nominally homogeneous sample may look heterogeneous when observed on short-time scales.

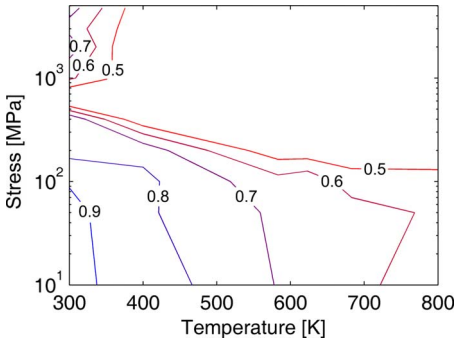

FIG. 8. (Color online) Contour plot of the localization index, Γ, for samples deformed at different combinations of applied stress and temperature. The region enclosed at high temperature and low applied stress corresponds to localization in large visible bands of concentrated shear, while the region enclosed at low applied stress is exhibited by small pockets of large strain in an otherwise uniformly deformed sample.

VI. EFFECTS OF PRE-EXISTING STRUCTURE

In the above discussion, all of the simulations began from a homogeneous, undeformed simulation cell (which we call "unequilibrated"). We now consider the effects of pre-existing structure by analyzing the same set of conditions on model glasses subjected to simulated thermal processing prior to loading.[37] These structures were formed by either (a) cooling at a rate of 10 K/s from an initial temperature of 1000 K or (b) equilibrating the system at the same temperature as the simulated mechanical test, as described in Ref. 37. Both these treatments have the effect of freezing in a distribution of stresses, with the "cooled" structure having the highest magnitude of residual stresses and the "equilibrated" structure having a lower magnitude of residual stresses.

These two thermally processed structures were subjected to the same 60 combinations of pure shear stress and temperature as the unequilibrated structure discussed above and followed over the course of 5000 STZ activations. In the analysis in Ref. 37, the cooled and equilibrated structures exhibited roughly the same overall strain rates as the unequilibrated structure, but the cooled and equilibrated structures never showed any macroscopically inhomogeneous deformation like the unequilibrated structure did. We performed the same analysis as provided in Secs. III–V on the cooled and equilibrated structures. This analysis led to almost identical results for the two, so here we discuss only the results for the cooled structure.

The distribution of pre-existing stresses in the cooled structure has the effect of broadening the distributions of $\rho(\Delta G)$ for the combinations of applied stress and temperature shown in Fig. 9. The distribution of $p(\Delta G)$, however, seems to be narrower for the cooled structure at lower energies when compared to the unequilibrated structure, which results from the long nonzero tails in the $\rho(\Delta G)$ distribution where the thermal energy dominates the probability for acti-

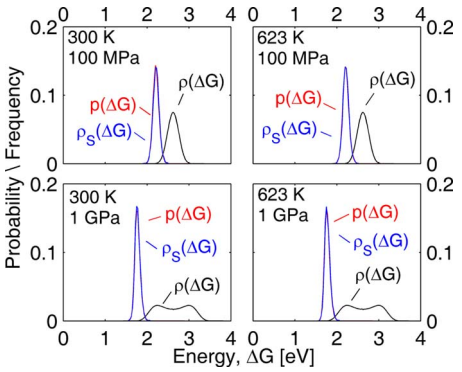

FIG. 9. (Color online) Statistics of the density of activation energies, $\rho(\Delta G)$, and the corresponding probability density distribution, $p(\Delta G)$, alongside the density of selected activation energies, $\rho_S(\Delta G)$, for four different simulations with pre-existing stresses (from a cooled structure), carried out under a combination of temperatures, 300 and 623 K, and applied stresses, 100 MPa and 1 GPa.

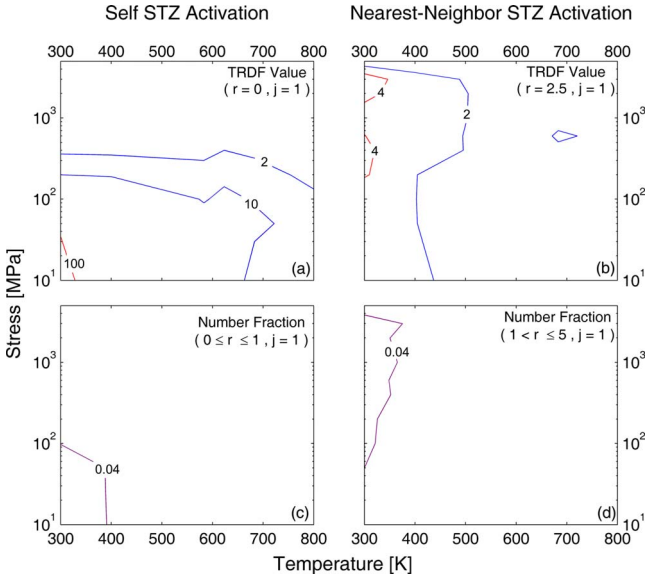

FIG. 10. (Color online) Contour plots of several different statistics of STZ correlations over a range of applied stresses and temperatures for a cooled structure with pre-existing stresses: (a) the TRDF values, $g(r,j)$, of self-STZ activation ($r=0$, $j=1$), (b) $g(r,j)$ of nearest-neighbor STZ activation ($r=2.5$, $j=1$), (c) number fraction of subsequent, $j=1$, self-STZ activation events within the range $0 \leq r \leq 1$, and (d) number fraction of subsequent nearest-neighbor STZ activation events within the range $1 < r \leq 5$.

vating these lower-energy transitions. Once again, $\rho_S(\Delta G)$ matches $p(\Delta G)$ almost exactly. However, the most important note to be made about the activation energies shown in Fig. 9 is that there is almost no change in the distributions from 623 to 300 K at the same applied stress. This means that the distribution of pre-existing stresses swamps out any low-energy transitions that might be created after the activation of a previous STZ, which would manifest more prominently in $p(\Delta G)$ at 300 K. In comparing these distributions at the two temperatures, there is little indication that the two simulations should behave differently as a result of the change in temperature.

The correlations in STZ activity for the cooled structure follow the same general trends that were seen in Fig. 4 for the unequilibrated structure. Figures 10(a) and 10(b) show the magnitude of $g(r,j)$ in an analogous manner to Fig. 5; comparison of these figures shows that the magnitudes for the peaks of the TRDFs of the cooled structure are much smaller than the peaks of the unequilibrated structure, although the same general regimes of behavior exist. The fraction of subsequent self-STZ activations, $j=1$, that occur within one STZ radius can be seen in Fig. 10(c), where it is noted that the region enclosed by the contours is much smaller than in Fig. 5(c); the distribution of pre-existing stresses (which are of a similar magnitude to those resulting from any single STZ activation) suppresses local self-activations. Similarly, the fraction of subsequent nearest-neighbor STZ activation events in the range of $r=1-5$, shown in Fig. 10(d), reflect a suppressed likelihood of observing correlated STZ activity in the presence of pre-existing stresses. Nevertheless, these correlations do exist at low temperatures in spite of the fact that the activation energy distributions suggest that the simulations should behave identically when deformed at the same stresses, no matter the temperature.

Perhaps the most interesting effect of the pre-existing stresses in the cooled structure is the lack of any macroscopic shear localization or inhomogeneous deformation, as mentioned previously and discussed in Ref. 37. There are small pockets of large strain throughout the structure following deformation, but nothing that would indicate a large degree of localization. In examining the value of the localization index, Γ, over the range of applied stresses and temperatures, it is nearly constant around 0.6, which is why it is not shown here. This lack of inhomogeneous response is consistent with the suppression of correlated STZ activity detailed in Fig. 10 for the cooled structure; we are now able to conclude that a significant internal stress distribution has a homogenizing influence on deformation at the level of individual STZs and consequently can suppress the formation of shear bands at larger scales. These results confirm the speculations proposed in Ref. 37 for the homogenizing effects of pre-existing stresses which make it difficult to observe perturbations of sufficient size that lead to localization. Similar effects are observed in atomistic simulations where differing pre-existing stress distributions can lead to or inhibit shear localization.[33] The results also rule out another possibility suggested in Ref. 37 that the small system size used in these simulations might in and of itself tend to suppress localization in a system with pre-existing perturbations. We believe that in order to observe localization in STZ dynamics simulations with realistic internal stress distributions, a local structural state variable, such as the free volume, is likely required. Recent results from atomistic simulations also suggest the need for a state variable beyond the stress state to more accurately account for the localized motion in metallic glasses.[46] This approach is frequently employed in mechanical models of amorphous systems[47] and provides a memory of the state (activation barriers) beyond the redistribution of stresses as is considered here. The development of such a model is left for future work.

VII. CONCLUSION

An analysis was performed on STZ dynamics simulation results[37] for deformation of a model amorphous metal. The goal of this analysis was to understand how STZs interact with one another at a microscopic level and how their collective operation combines to effect deformation on a macroscopic level. A statistical analysis of the activation energies of the ensemble of potential STZs and their corresponding probabilities illustrates the influence of applied stress and temperature on the transitions that are most likely to be activated. Specifically, a trend from allowing STZs to shear in a number of directions at high temperatures and low stresses transitions to a trend for STZs to shear in only one direction at low temperature and high applied stress. Finally, a comparison of the probabilities of the potential transitions to the transitions which were selected during the simulations shows excellent agreement.

An analysis of the distance and time between STZ activations elucidates three general behaviors, identified as nearest-neighbor, independent, and self-STZ activations. The nearest-neighbor STZ activation behavior occurs at low temperature and high applied stress and indicates that a subsequent STZ activation is likely to occur in the immediate neighborhood of the first. The independent STZ activation behavior occurs at high temperatures and any applied stress and indicates that the preference for activating any one of the potential STZs is independent of its location relative to previous activations. Finally, the self-STZ activation behavior occurs at low temperatures and low stresses and predicts that a subsequent STZ will have to activate in very close proximity to (i.e., atop) the previous STZ to relax the system locally. The temporal components of the STZ correlations are found to be short-lived, always falling off after about five STZ activations.

These three behaviors have been mapped onto an STZ correlation map and matched with their corresponding macroscopic mode of deformation, which are inhomogeneous, homogeneous, and elastic, respectively. These regions are also corroborated by macroscopic observations of the degree of homogeneity in the deformation, which we quantify with a "localization index." Interestingly, we find that having preexisting structure in the simulation cell, in the form of a distribution of internal stresses and strains such as are expected for amorphous materials, diminishes the ability of the STZs to communicate with one another through stress redistribution. As a result, both microscopic and macroscopic localization are suppressed in such systems and true localization (i.e., shear banding) only occurs in systems without preexisting structure.

ACKNOWLEDGMENTS

This work was primarily supported by the U.S. Office of Naval Research under Contract No. N00014-08-1-0312. E.R.H. gratefully acknowledges support through the National Defense Science and Engineering Graduate (NDSEG) Foundation with support from the Army Research Office (USARO). Correspondence with V. V. Bulatov regarding his work in Ref. 35 is gratefully acknowledged.

APPENDIX: CALCULATION OF THE ACTIVATED STATE

Consider an elementary reaction, the simple shearing of an STZ through a defined increment of strain γ_o, as shown in Fig. 2(a). The value of the local plastic strain γ_p (defined parallel to a given shear plane) is incremented as

$$\gamma_p^F = \gamma_p^I + \gamma_o, \tag{A1}$$

where the superscripts I and F represent the initial and final values, respectively. There is a corresponding variation in elastic energy from the energy in the initial state, E^I, to the energy in the final state, E^F. This variation in elastic energy, which is a quadratic function of γ_p,[48] can be calculated analytically for an idealized STZ using the Eshelby solution for an elastic inclusion[49] or can be evaluated numerically by visiting the final state following the transition.

A traditional KMC model uses the energy change to model the activation energy, ΔG, by adding a barrier of fixed height, ΔF, to the average of E^I and E^F, as illustrated in Fig. 2(b). This approach satisfies detailed balance for the reaction because a forward transition traverses the same activated state as the reverse transition

$$E^I + \Delta G_{I\to F} = E^F + \Delta G_{F\to I}, \tag{A2}$$

with $\Delta G_{I\to F}=(E^F-E^I)/2+\Delta F$ and $\Delta G_{F\to I}=(E^I-E^F)/2+\Delta F$. However, this conventional approach of calculating ΔG is not well suited to an STZ dynamics model; it requires calculation of the energy in the final state, which is both computationally expensive for a large number of possible transitions and essentially impossible for continuously distributed shearing angles as used in the present model.

Bulatov and Argon[35] exploited the property that the elastic energy, and therefore the total energy as well, is a quadratic function of γ_p to provide an alternate formulation for ΔG. This quadratic variation in energy is shown in both Figs. 2(b) and 2(c), illustrating that the system evolution is independent of the model for the activated state. It can be shown that the local shear stress resolved in the shear plane of γ_p is given by the slope of the variation in energy

$$\tau = -\frac{1}{\Omega_o}\frac{\partial E}{\partial \gamma_p} = -\frac{E'(\gamma_p)}{\Omega_o}. \tag{A3}$$

Given Eq. (A3), ΔG for the transition, as defined in Eq. (2) and illustrated in Fig. 2(c), is determined by projecting with the slope, τ^I, from the energy of the initial state to the midpoint of the reaction, $\frac{1}{2}\gamma_o$ (energy variation $-\frac{1}{2}\tau^I\Omega_0\gamma_0$), and

then adding the fixed barrier height, ΔF. Detailed balance for this model of ΔG is satisfied because

$$E^I + \left(\Delta F - \tfrac{1}{2}\tau^I \Omega_o \gamma_o\right) = E^F + \left[\Delta F - \tfrac{1}{2}\tau^F \Omega_o(-\gamma_o)\right], \quad \text{(A4)}$$

which follows a property of quadratic functions that $E(\gamma^I) + E'(\gamma^I)(\gamma^F - \gamma^I)/2 = E(\gamma^F) - E'(\gamma^F)(\gamma^F - \gamma^I)/2$. This is illustrated in Fig. 2(c) by the fact that the tangents to the variation in energy at the initial and final states, τ^I and τ^F, respectively, cross exactly at $\frac{1}{2}\gamma_o$.

*On sabbatical leave from the Institut Polytechnique, Grenoble, France.
†Corresponding author; schuh@mit.edu

[1] C. A. Schuh, T. C. Hufnagel, and U. Ramamurty, Acta Mater. **55**, 4067 (2007).
[2] F. Spaepen, Acta Metall. **25**, 407 (1977).
[3] A. S. Argon, Acta Metall. **27**, 47 (1979).
[4] A. S. Argon and L. T. Shi, Acta Metall. **31**, 499 (1983).
[5] M. L. Falk and J. S. Langer, Phys. Rev. E **57**, 7192 (1998).
[6] J. S. Langer, Phys. Rev. E **64**, 011504 (2001).
[7] W. L. Johnson and K. Samwer, Phys. Rev. Lett. **95**, 195501 (2005).
[8] M. D. Demetriou, J. S. Harmon, M. Tao, G. Duan, K. Samwer, and W. L. Johnson, Phys. Rev. Lett. **97**, 065502 (2006).
[9] K. Maeda and S. Takeuchi, Phys. Status Solidi A **49**, 685 (1978).
[10] A. S. Argon and H. Y. Kuo, Mater. Sci. Eng. **39**, 101 (1979).
[11] S. Kobayashi, K. Maeda, and S. Takeuchi, Acta Metall. **28**, 1641 (1980).
[12] D. Deng, A. S. Argon, and S. Yip, Philos. Trans. R. Soc. London, Ser. A **329**, 595 (1989).
[13] C. Maloney and A. Lemaitre, Phys. Rev. Lett. **93**, 195501 (2004).
[14] A. Tanguy, F. Leonforte, and J. L. Barrat, Eur. Phys. J. E **20**, 355 (2006).
[15] C. E. Maloney and A. Lemaître, Phys. Rev. E **74**, 016118 (2006).
[16] P. Schall, D. A. Weitz, and F. Spaepen, Science **318**, 1895 (2007).
[17] D. Rodney and C. Schuh, Phys. Rev. Lett. **102**, 235503 (2009).
[18] A. S. Argon and L. T. Shi, Philos. Mag. A **46**, 275 (1982).
[19] L. O. Eastgate, J. S. Langer, and L. Pechenik, Phys. Rev. Lett. **90**, 045506 (2003).
[20] M. L. Falk, J. S. Langer, and L. Pechenik, Phys. Rev. E **70**, 011507 (2004).
[21] L. Anand and C. Su, J. Mech. Phys. Solids **53**, 1362 (2005).
[22] G. Picard, A. Ajdari, F. Lequeux, and L. Bocquet, Phys. Rev. E **71**, 010501 (2005).
[23] L. Anand and C. Su, Acta Mater. **55**, 3735 (2007).
[24] E. A. Jagla, Phys. Rev. E **76**, 046119 (2007).
[25] L. Bocquet, A. Colin, and A. Ajdari, Phys. Rev. Lett. **103**, 036001 (2009).
[26] J. Lu, G. Ravichandran, and W. L. Johnson, Acta Mater. **51**, 3429 (2003).
[27] H. Neuhauser, Scr. Metall. **12**, 471 (1978).
[28] P. E. Donovan and W. M. Stobbs, Acta Metall. **29**, 1419 (1981).
[29] E. Pekarskaya, C. P. Kim, and W. L. Johnson, J. Mater. Res. **16**, 2513 (2001).
[30] T. C. Hufnagel, T. Jiao, Y. Li, L. Q. Xing, and K. T. Ramesh, J. Mater. Res. **17**, 1441 (2002).
[31] R. D. Conner, W. L. Johnson, N. E. Paton, and W. D. Nix, J. Appl. Phys. **94**, 904 (2003).
[32] R. D. Conner, Y. Li, W. D. Nix, and W. L. Johnson, Acta Mater. **52**, 2429 (2004).
[33] Y. Shi and M. L. Falk, Phys. Rev. Lett. **95**, 095502 (2005).
[34] Y. Shi and M. L. Falk, Scr. Mater. **54**, 381 (2006).
[35] V. V. Bulatov and A. S. Argon, Modell. Simul. Mater. Sci. Eng. **2**, 167 (1994).
[36] J.-L. Barrat and J. J. de Pablo, MRS Bull. **32** (11), 941 (2007).
[37] E. R. Homer and C. A. Schuh, Acta Mater. **57**, 2823 (2009).
[38] E. Lerner and I. Procaccia, Phys. Rev. E **79**, 066109 (2009).
[39] J. C. Baret, D. Vandembroucq, and S. Roux, Phys. Rev. Lett. **89**, 195506 (2002).
[40] R. C. Tolman, *The Principles of Statistical Mechanics* (Oxford University Press, Oxford, 1938).
[41] A. Voter, in *Radiation Effects in Solids*, edited by K. E. Sickafus, E. A. Kotomin, and B. P. Uberuaga (Springer, NATO Publishing Unit, Dordrecht, The Netherlands, 2006), pp. 1–24.
[42] J. G. Amar, Comput. Sci. Eng. **8**, 9 (2006).
[43] A. B. Mukhopadhyay, C. Oligschleger, and M. Dolg, J. Phys. Chem. B **108**, 16085 (2004).
[44] F. Leonforte, R. Boissiere, A. Tanguy, J. P. Wittmer, and J. L. Barrat, Phys. Rev. B **72**, 224206 (2005).
[45] Y. C. Fung and P. Tong, *Classical and Computational Solid Mechanics* (World Scientific, Singapore, 2001).
[46] M. Tsamados, A. Tanguy, F. Leonforte, and J. L. Barrat, Eur. Phys. J. E **26**, 283 (2008).
[47] A. Lemaitre, Phys. Rev. Lett. **89**, 195503 (2002).
[48] T. Mura, *Micromechanics of Defects in Solids* (Nijhoff, Dordrecht, 1987).
[49] J. D. Eshelby, Proc. R. Soc. London, Ser. A **241**, 376 (1957).